Applied Surface Science 713 (2025) 164274

Contents lists available at ScienceDirect

Applied Surface Science

journal homepage: www.elsevier.com/locate/apsusc

Full Length Article

Insights into surface microstructural engineering of Inconel 625 for enhanced oxygen evolution reaction performance

Luka Suhadolnik [a,*], Črtomir Donik [b], Blaž Tomc [a], Mejrema Nuhanović [a], Martin Šala [a], Marjan Bele [a], Matjaž Finšgar [c], Andraž Mavrič [d], Iztok Arčon [d], Matjaž Godec [b], Nejc Hodnik [a,b,**]

[a] Department of Materials Chemistry, National Institute of Chemistry, Hajdrihova 19, SI-1000 Ljubljana, Slovenia
[b] Institute of Metals and Technology, Ljubljana, Slovenia
[c] Faculty of Chemistry and Chemical Engineering, University of Maribor, Smetanova ulica 17, Maribor 2000, Slovenia
[d] University of Nova Gorica, Vipavska 13, SI-5000 Nova Gorica, Slovenia

ARTICLE INFO

Keywords:
Electrocatalysis
Compositionally complex materials
Commercial nickel alloys
Oxygen evolution reaction
Scanning electron microscopy
IL-SEM

ABSTRACT

This study demonstrates the transformation of commercially produced Inconel 625, a Ni-based superalloy, into a high-performance oxygen evolution reaction (OER) anode material through sequential nitridation and anodic oxidation treatments. Nitridation at 750 °C enriches surface NiFe content at the grain boundaries and scratches while reducing Cr concentration. Subsequent anodic oxidation further aggressively restructures the surface, introducing micrometer-scale cracks through aggressive intergranular corrosion, where the regions with smaller grains exhibit enhanced porosity. Through these surface modifications, an 8:1 NiFe ratio is established as an active OER oxyhydroxide film. Nano-to-microscale morphological and compositional insights are revealed through an advanced electrochemical characterization approach, utilizing identical location (IL) electron microscopy techniques, including IL-scanning electron microscopy and IL-energy dispersive spectroscopy mappings, along with time-of-flight secondary ion mass spectrometry, X-ray photoelectron spectroscopy and Fe and Ni K-edge X-ray absorption spectroscopy. The treated Inconel 625 exhibits a twofold increase in electrochemical surface area and outperforms both the untreated analog and iridium-based benchmark in OER performance. These findings establish Inconel 625 as a scalable and cost-effective material for alkaline water electrolyzers. Advanced surface engineering of complex alloys offers a promising route to address key electrocatalytic challenges and drive the hydrogen economy forward.

1. Introduction

Global warming and the urgent need for renewable energy sources have intensified the search for efficient and sustainable methods to store and utilize clean energy [1]. Hydrogen, produced through water electrolysis, offers a promising solution for energy storage, a concept known as the hydrogen economy [2]. Alkaline water electrolysis is among the oldest and most mature technologies for hydrogen production, with roots tracing back over a century. It operates by splitting water via hydrogen and oxygen evolution reactions (HER and OER) using an alkaline electrolyte, typically 30 % potassium hydroxide (KOH) water solution, and has been deployed at an industrial scale since the early 20th century. The design of alkaline electrolyzers closely mirrors that of the chloralkali process, sharing commonalities in both cell structure and electrode materials. In both cases, Ni is considered a state-of-the-art material in the form of an OER active film formed on a mesh-type Ni anode to facilitate gas transport and, at the same time, also enlarge the surface area. These bulk metallic electrodes must balance high conductivity, chemical stability, and mechanical durability while operating under strongly alkaline and oxidizing conditions.

NiFe-based oxyhydroxides ($Ni_{1-x}Fe_xOOH$) have emerged as promising candidates for OER catalysis due to their earth-abundance and cost-effectiveness. These materials are particularly useful in alkaline water electrolyzers, where their performance is significantly influenced by the Fe/Ni ratio, typically ranging between 0.11 and 1 [3–8]. Despite their potential, several challenges remain. The nature of the active sites

* Corresponding author.
** Corresponding author at: Department of Materials Chemistry, National Institute of Chemistry, Hajdrihova 19, SI-1000 Ljubljana, Slovenia.
E-mail addresses: luka.suhadolnik@ki.si (L. Suhadolnik), nejc.hodnik@imt.si (N. Hodnik).

https://doi.org/10.1016/j.apsusc.2025.164274
Received 16 June 2025; Received in revised form 31 July 2025; Accepted 5 August 2025
Available online 6 August 2025
0169-4332/© 2025 The Author(s). Published by Elsevier B.V. This is an open access article under the CC BY license (http://creativecommons.org/licenses/by/4.0/).

in $Ni_{1-x}Fe_xOOH$, whether Fe atoms, Ni atoms, or a synergy between the two, continues to be debated. Some studies suggest that Fe atoms within a Ni oxo-hydroxide matrix are the primary active sites, with the matrix providing essential support in terms of electrical conductivity, chemical stability, and surface area. The synthesis of NiFe-based electrocatalysts often involves co-precipitation, homogeneous precipitation, or electrodeposition, which allows for crystal size and morphology tailoring. However, their long-term operational stability can be limited by poor adhesion to support materials or the degradation of the support itself, posing a significant barrier to industrial application.

Bulk commercial stainless steels and other compositionally complex alloys (CCAs) containing Ni and Fe have demonstrated significant potential as anode materials for OER [3]. Activation methods, such as applying high current in alkaline electrolytes or cyclic treatments between high and low potentials, have induced stable, catalytically active surface layers. Research indicates that the Fe/Ni ratio in the resulting NiFe oxyhydroxide layer is critical in determining OER performance, with an optimal range between 0.2 and 0.4. Alloys with initially low Fe content benefit from Fe incorporation during electrochemical aging, while Fe-rich alloys tend to form Ni-enriched surface layers, leading to enhanced catalytic activity. Notably, regardless of the alloy's initial composition, electrochemical aging typically results in forming a similar NiFe-based OER-active layer, with a thickness of approximately 10–50 nm. Interestingly, Inconel 625 had the thickest active surface layer (38.8 $\pm$ 2.7 nm) among the samples studied [3]. Because Ni content is the primary cost driver for steel, the goal is to reduce Ni content as much as possible while preserving high OER activity, given nickel's relatively high price and potentially limited availability.

Inconel 625 is interesting due to its Ni-rich composition, approximately 60 % Ni, 20 % Cr, 5 % Fe, 10 % Mo, and trace elements (e.g., 1–2 % Nb). These Ni-Cr-based superalloys are commercially available and still relatively cost-effective for use in alkaline water electrolyzers, where, for instance, a medium-sized alkaline electrolyzer with an anode surface area of 1 m^2 and an anode thickness of 1 mm, made of Inconel 625, is approximately 150 $ (in 2025). This would represent a small fraction of the costs associated with a 1 m^2 alkaline water electrolyzer, including the balance of plant well above 20,000 $ (in 2025). Interestingly, the same size anode made from 304 type stainless steel, containing 70 % Fe, 8–10.5 % Ni, 18–20 % Cr, $\leq$2% Mn, would cost roughly 36 $. However, this is approximately a five times reduction in anode price, which does not affect the price of the electrolyzer system. Although both Inconel 625 and various stainless steels are high-performance alloys, Inconel 625 exhibits higher oxidation and corrosion resistance in highly corrosive media.

The anodic OER, a critical half-reaction in water electrolysis, remains a major bottleneck due to its sluggish kinetics and high overpotentials, which significantly limit overall system efficiency [9]. Traditional OER electrocatalysts, such as iridium oxide and Raney nickel coatings, are relatively effective but are limited in availability and, in the case of iridium, have extremely high cost, highlighting the need to minimize their use or replace them with sustainable, high-performance alternatives. Furthermore, enhancing their performance without sacrificing stability requires innovative surface engineering strategies beyond conventional coatings or nanoparticle depositions. The scientific and innovation communities must adopt new conceptual approaches to achieve this. The traditional trial-and-error optimization of well-known catalysts has reached its limits and no longer yields breakthroughs. Therefore, the focus must shift toward novel materials, such as CCAs. These materials, composed of multiple metal elements similar to high entropy alloys (HEA), can form a diverse range of surface sites with tunable properties, which may exhibit optimal intrinsic activity for the OER [10].

Moreover, combining compositional versatility with structurally diverse features, such as defects, opens new avenues for fine-tuning electrocatalytic surfaces beyond traditional CCAs and HEAs. State-of-the-art electrocatalysis research has traditionally focused on surface and near-surface composition or atomic structure using platforms like single crystals [11] or nanoparticles [12] or recent sputtered materials libraries [13], to identify theoretical and experimental activity descriptors describing structure–function relationships, such as the d-band center or work function [12,14–16]. However, these approaches often neglect a wide range of structural and compositional defects ubiquitous in real metal-based anodes. These include point defects, dislocations, twin boundaries, grain characteristics (e.g., size, shape, orientation, and strain), grain boundaries, precipitates, and larger features like cracks and pits, which can affect both activity and stability of electrocatalysts [17–19]. Grain boundaries are often formed between regions of dissimilar compositions, creating complex electrochemical environments, namely defects, that can significantly impact catalytic performance [20]. While single-crystal electrodes offer characterization of individual surface phenomena, they fail to capture the intricate interactions and combined effects of coexisting surface types typical of polycrystalline materials. Oversimplifying these systems and ignoring such structural complexity limits our understanding of the actual behavior of bulk metal-based electrodes. Despite their well-established importance in metallurgy [21] and corrosion science, the effects of structural defects on electrocatalytic behavior remain underexplored. Even subtle microstructural changes can dramatically alter mechanical and chemical properties [21]. Such know-how in steel metallurgy was obtained in centuries of trial-and-error experiments, due to the great complexity, the fundamental mechanisms still remain imperfectly explained. In electrocatalysis, details such as specific defects of nanoparticles were shown to significantly affect the catalyst's performance [12,22].

The broad spectrum of defects in bulk metallic surfaces thus represents a major opportunity for enhancing electrocatalyst performance and lifetime. For instance, grain boundary engineering is becoming popular in boosting electrocatalysis [23]. However, it introduces considerable complexity, making systematic investigation extremely challenging, if not impossible. This complexity is why literature lacks studies examining locally resolved discrepancies in the nano-to-microscale surface morphology and composition of electrocatalytic metals. While it is well established that metals comprise grains, grain boundaries, and complex metallic phases, even alloys with homogeneous compositions can exhibit significant local variations. As demonstrated before, nanoparticulate electrocatalysts exhibit great structural complexity, leading to complex atomic-level changes [20,21], each nanoparticle possessing a unique atomic structure [24]. Thus, the only way to explore these systems is to study each nanoparticle individually and track how it changes with the operation time, referred to as the bottom-up approach [22]. Similarly to nanoparticles, polycrystalline bulk electrodes inherently possess heterogeneous surfaces of different grains. This makes it essential to investigate the electrochemical behavior of individual grains, sites, and defects and their synergistic interactions, the concept known as single-entity electrochemistry (SEE) [25]. To address this challenge, advanced local electrochemical techniques, such as electrochemical identical-location electron microscopy (IL-EM) [26], also referred to as Nano Lab [26], offer a unique capability to track morphological, compositional, and structural changes at selected sites with SEM and down to the atomic level with transmission electron microscopy (TEM).

While efficiency is undoubtedly important for minimizing energy losses in electrolysis, an excessive focus on achieving extreme efficiency can inadvertently drive up costs in terms of advanced equipment and the use of precious group metals while increasing system complexity. This trade-off can ultimately impede large-scale deployment. We argue that a more balanced approach is needed, considering both efficiency and affordability, scalability, and long-term stability. In this context, the scalability and low cost of Fe-containing alloys like steel make them a compelling candidate for repurposing as an anode material in alkaline OER systems, offering a practical and economically viable path forward for industrial-scale alkaline water electrolysis. As such, alkaline electrolysis holds significant promise for widespread adoption, whereas

proton exchange membrane (PEM) electrolysis may remain limited to niche applications where low system weight is a critical requirement [27].

In this study, we investigated the catalytic potential of Inconel 625 for the oxygen evolution reaction (OER) in alkaline media, building upon previous research that highlights the promise of various NiFe-containing compositionally complex material (CCM)-based catalysts. Two key unresolved questions remain: First, how can Inconel 625 be activated to further enhance the catalytic activity of the surface layer? This is particularly relevant because the alloy's inherent corrosion resistance, beneficial in many industrial applications, can hinder electrocatalytic performance due to surface passivation, which limits the availability of active sites. To address this limitation, we implemented an advanced activation strategy combining thermal nitridation and electrochemical anodic oxidation to enhance both the surface area and intrinsic catalytic activity. The second, more fundamental question concerns how Inconel 625 behaves at the nano- to microstructural level during surface treatments and OER operation. Previous studies primarily assessed bulk or averaged surface properties, such as average NiFe oxyhydroxide film composition and thickness, using techniques such as X-ray photoelectron spectroscopy (XPS) and X-ray absorption spectroscopy (XAS), without accounting for local structural variations. In contrast, our study reveals how microstructural features, such as grain size, grain boundaries, and segregated regions, evolve during activation and OER cycling. To uncover these localized changes, we employed a suite of advanced characterization techniques, including IL-SEM, electron backscatter diffraction (EBSD), energy dispersive spectroscopy (EDS), XPS, and time-of-flight secondary ion mass spectrometry (ToF-SIMS). This comprehensive approach enables tracking compositional and morphological transformations with nanoscale resolution and gaining insight into catalytic behavior's structural origins. We observed that the initial surface state and only thermal treatment of Inconel 625 provide limited OER enhancement. However, anodic oxidation effectively increases the active surface area, partially removes Cr, and optimizes the NiFe ratio in the OER active oxo-hydroxide layer to approximately 8:1. This tailored surface engineering achieves OER performance that surpasses commercial IrO_2. By refining these activation parameters, we successfully transformed Inconel 625 into a scalable and cost-effective NiFe-based oxygen-evolving electrode, demonstrating a broader concept for converting NiFe-containing alloys into efficient anodes with substantial potential for application in industrial alkaline water electrolyzers.

2. Experimental

2.1. Sample preparation

IN625 was machined into flat disc-shaped samples with a diameter of 5 mm and a height of 3 mm. Then metallic samples were mechanically ground and polished following a standard metallographic procedure. First, specimens were ground using SiC abrasive papers with progressively finer grit sizes (typically from #320 to #1200) under running water to minimize heat generation. Subsequent polishing was carried out using diamond suspensions of decreasing particle sizes (9 μm, 3 μm, and 1 μm) on appropriate polishing cloths. The final polishing step was performed using a colloidal silica suspension (OP-S, ~0.04 μm) for approximately 15 min to obtain a deformation-free and highly reflective surface suitable for SEM and EBSD analysis. Between each polishing step, the samples were thoroughly rinsed with ethanol and dried with compressed air to avoid cross-contamination.

2.2. Characterization methods

Surface morphology and compositional analysis were performed at the National Institute of Chemistry, Ljubljana, Slovenia. Scanning electron microscopy (SEM) was conducted using a Thermo Fisher Scientific Apreo field emission scanning electron microscope (FE-SEM), operated at an accelerating voltage of 10–20 kV. Imaging was carried out in both secondary electron (SE) and backscattered electron (BSE) modes to assess surface topography and compositional contrast. Elemental analysis was performed using an energy-dispersive X-ray spectrometer (EDS) equipped with a silicon drift detector (SDD) Ultim Max 100 (Oxford Instruments, Oxford, UK).

At the Institute of Metals and Technology, Zeiss CrossBeam 550 field-emission scanning electron microscope (FIBSEM), produced by Carl Zeiss in Oberkochen, Germany, was utilised for the in-depth analyses performed in this study. This microscope features an EDAX Hikari Super electron-backscatter diffraction (EBSD) camera, which is crucial for delivering high-resolution crystallographic data. It utilises APEX software for thorough compositional analyses and EBSD for phase mapping. A wide array of parameters was selected to ensure the acquisition of the most accurate and relevant results during the imaging and analysis phases. Specifically, an accelerating voltage of 15 kV was applied, accompanied by a probe current between 2.0 and 5.0nA, allowing for high-quality secondary electron images that illustrate the microstructural characteristics of the samples. Together with EBSD, using 15 kV and 10nA, crystallographic properties and phases were effectively determined.

Spherical indexing was employed to extract crystallographic orientation data with improved accuracy, particularly in low-quality or deformed regions. For the post-processing of low-intensity Kikuchi patterns from thick(er) films, which cannot be adequately analysed and characterised using a simple Hough transformation, EDAX OIM 9 has been utilised with spherical indexing. This method allowed for robust orientation mapping with enhanced precision over conventional Hough-based techniques, especially beneficial for fine-grained or plastically deformed microstructures. Post-processing included grain boundary detection, misorientation analysis, and noise reduction using standard cleanup routines.

X-ray photoelectron spectroscopy (XPS) measurements were performed using a Kratos Supra+ instrument (Manchester, UK) equipped with an Al K_α radiation source. The binding energy was corrected using the C–C/C–H peak in the C 1s spectrum set to 284.8 eV. Samples were affixed to the sample holder using double-sided Si-free tape. Spectra acquisition was carried out at a 90° take-off angle, targeting an analysis area of 300 by 700 μm. The pass energy was configured to 160 eV for survey spectra and 20 eV for high-resolution spectra. Data acquisition and processing were executed using Kratos ESCApe 1.5 software.

Time-of-flight secondary ion mass spectrometry (ToF-SIMS) analyses were conducted using an M6 instrument (IONTOF, Münster, Germany). Measurements were performed in negative polarity. For 3D ToF-SIMS imaging, a 2 keV Cs^+ sputter beam was applied over a 500 by 500 μm area for 3 h, while data acquisition was carried out with a 30 keV Bi^+ primary ion beam focused on a 300 by 300 μm region in the middle of the sputter crater. The acquired spectra were processed and analyzed using SurfaceLab 7.4 software.

The main objective of X-ray absorption spectroscopy (XAS) measurements was to determine the valence state of constituent Fe and Ni cations in a catalyst film formed on the surface of the samples after nitridation and anodic oxidation. To distinguish the structure of the OER oxyhydroxide film, we performed XAS measurements in total electron yield (TEY) detection mode. Due to the low penetration depth of photo-excited electrons, TEY detection mode allows measurements of XAS spectra of predominantly the surface layer of about 100 nm.

The XAS experiments were performed at the SAMBA beamline of the SOLEIL synchrotron radiation facility in Paris on pristine and treated samples. A Si(220) double crystal monochromator was used (a first flat water-cooled crystal and a sagittal bent 2nd crystal) with an energy resolution of about 1 eV at 8 keV. The size of the beam on the sample was set to about 300 μm × 300 μm. Sample disks were glued with conductive silver paste on the sample holder. TEY detection mode measurements were done in a vacuum chamber at pressures below 10–5 mbar. The

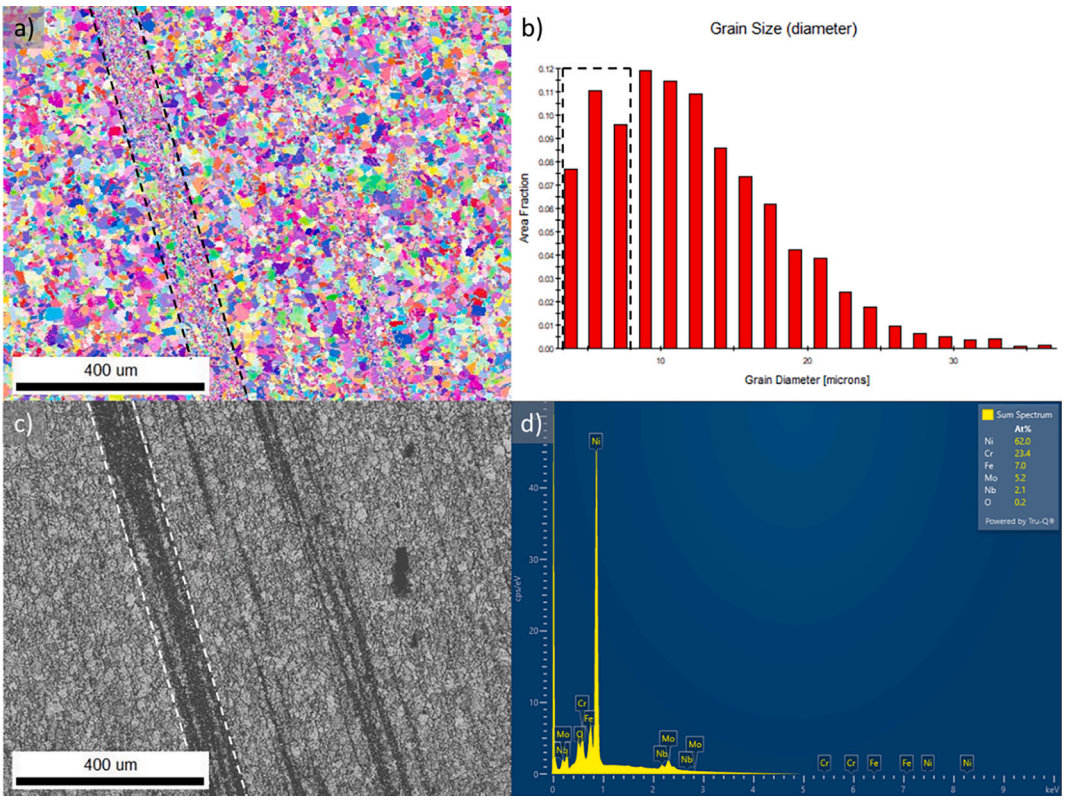

Fig. 1. Microstructural characterization of polished Inconel alloy surface: a) EBSD, b) grain size distribution, c) SEM backscatter image, and d) EDS spectrum of the identical surface region. Fig. c) shows white dashed lines representing a region with smaller grains, also referred to as segregation regions.

incident monochromatic X-ray beam was orthogonal to the sample surface. The XAS spectra were measured in the energy range of the Fe and Ni K-edges in each sample, on the same spot on each sample, i.e. without moving the sample. The beam position on the sample was stable within a few microns. The XAS scans were performed in the energy range from −150 eV to + 1000 eV relative to the K-edge of the investigated element, with a velocity of 10 eV/s and an energy step of 0.25 eV. To improve the signal-to-noise ratio, 10 repetitions of each scan were collected. The exact energy calibration was established with absorption measurement on a 5-μm thick Fe or Ni metal foil. The absolute energy reproducibility of the measured spectra was ± 0.03 eV.

The analysis of XANES spectra is performed with the Demeter (IFEFFIT) program package in combination with the FEFF6 program code for ab initio calculation of photoelectron scattering paths [28]. Fe and Ni K-edge XANES analysis was used to determine the valence states of the constituent metals in the 100 nm surface layer of the pristine samples and samples after nitridation and anodic oxidation. The Fe and Ni K-edge XANES spectra of pristine Inconel 625 and after nitridation and anodic oxidation (n + ao) are shown in Figs. XANES1 and XANES2, together with spectra of the reference Fe and Ni compounds. Different oxidation states and local environments of Fe and Ni cations lead to different Fe and Ni K-edge profiles and K-edge energy positions. The energy position of the Fe and Ni K-edges correlates with the valence state of the Fe and Ni cations in the sample [29–31]. The energy of the Fe and Ni K-edge of the is shifted to higher energies by 4 eV and 2 eV per valence state, respectively.

When the sample contains the same cation in two or more chemical states with different valence states and local structures, then the measured XANES spectrum is a linear combination of individual XANES spectra of the individual cation states. In such cases, a linear combination fit can provide very precise information about the relative amounts of the cation in each valence state. In our case, we determined relative amounts of different valence states of each investigated metal cation in the samples by a linear combination fit with a set of reference XANES spectra measured on selected reference compounds with known valence states and local structure of the investigated element. In this way, we identified different valence states of the investigated metal cations and determined the relative amounts of cations in each valence state in about a 100 nm thick surface layer of the samples before and after the treatment (nitridation and anodic oxidation). Results of LCF XANES analysis for Fe and Ni in the Inconel sample before and after the treatment are presented in Table S1 below.

All electrochemical measurements were conducted at ambient temperature in a single-compartment electrochemical cell equipped with a three-electrode configuration. Unmodified and activated Inconel 625 samples were mounted in a custom-made Teflon holder and used as the working electrode. A Hg/HgO reference electrode and a nickel wire coil as the counter electrode were employed. The electrolyte was 1 M KOH (Titripur, Merck), continuously purged with oxygen throughout the measurements. Linear sweep voltammetry (LSV) was used to assess OER activity performed at a scan rate of 2 mV s^{-1}. Electrochemical impedance spectroscopy (EIS) measurements were performed at OER potential of 1.55 V vs. RHE in the frequency range between 100 kHz and 1 Hz with an amplitude of 10 mV. The potentiostat used was a Biologic SP-300, and 85 % iR compensation was applied in all measurements.

IrO_2 benchmark preparation: A thin film of commercial IrO_2 powder (Alfa Aesar) was deposited on a glassy carbon rotating disk electrode (RDE) with a catalyst loading of 102 μg/cm^2. The film was prepared by drop-casting 20 μL of an ink composed of IrO_2 nanoparticles dispersed in a 7:1 mixture of water and 2-propanol. The ink pH was adjusted to 11 using 1 M KOH. A 5 % Nafion stock solution (Aldrich) was added to achieve a Nafion content of 25 wt% relative to the total solids in the suspension.

Table 1
Atomic concentrations (in %) of different elements in Inconel 625 measured with EDS.

element	at.% before treatment	After nitridation	After AO	After OER
Ni	62.1	56.1	45.4	40.7
Cr	23.6	12.0	9.9	7.2
Fe	6.8	6.1	5.9	6.3
Mo	4.9	3.3	/	2.0
Nb	2.0	1.3	1.1	1.4
O	0.5	3.3	15.5	30.3
N	/	18.1	14.2	n.d.
F	/	n.d.	7.9	n.d.

3. Results and discussion

3.1. Microstructural analysis of polished Inconel 625 surface

Polished Inconel 625 predominantly exhibits well-defined grains with distinct boundaries, as revealed by EBSD and SEM backscatter imaging (Fig. 1a,c). Grain size distribution analysis confirms a predominantly uniform grain structure (Fig. 1b), although ~ 10 % of the surface features smaller grains in a marked area with dashed lines (marked on Fig. 1a,c), formed due to segregation during alloy thermal treatment. These microstructural variations are expected to influence the material's properties, including its susceptibility to subsequent surface treatments, as discussed in later sections. More examples of microstructural EBSD and SEM backscatter analysis are shown in the Supplementary Information (Fig. S1).

EDS analysis (Fig. 1d and Table 1) and elemental mapping (Fig. 2) of the untreated Inconel 625 surface reveal that the constituent metals are generally evenly distributed across grain interiors and boundaries. Closer inspection indicates the presence of localized precipitates enriched in Cr, Mn, and Nb carbides or oxides (marked with white arrows) and slight compositional variations in Nb and Mo across the surface (marked with white dashed lines), which are typical features for Inconel. XRD analysis (Fig. S2) reveals typical Inconel 625 diffractions, corresponding to the face-centered cubic (FCC) Ni-Cr solid solution phase [32].

3.2. Effects of nitridation

Nitridation at 750 °C for 30 min in NH_3 atmosphere induced localized precipitation at grain boundaries and surface defects such as scratches (Fig. 3) as confirmed by IL-SEM imaging of the identical location of Inconel surface before and after nitridation (Fig. 3a,b). The locations of the formation of secondary phases on the grain boundaries are highlighted by yellow dashed lines and scratches by the red line

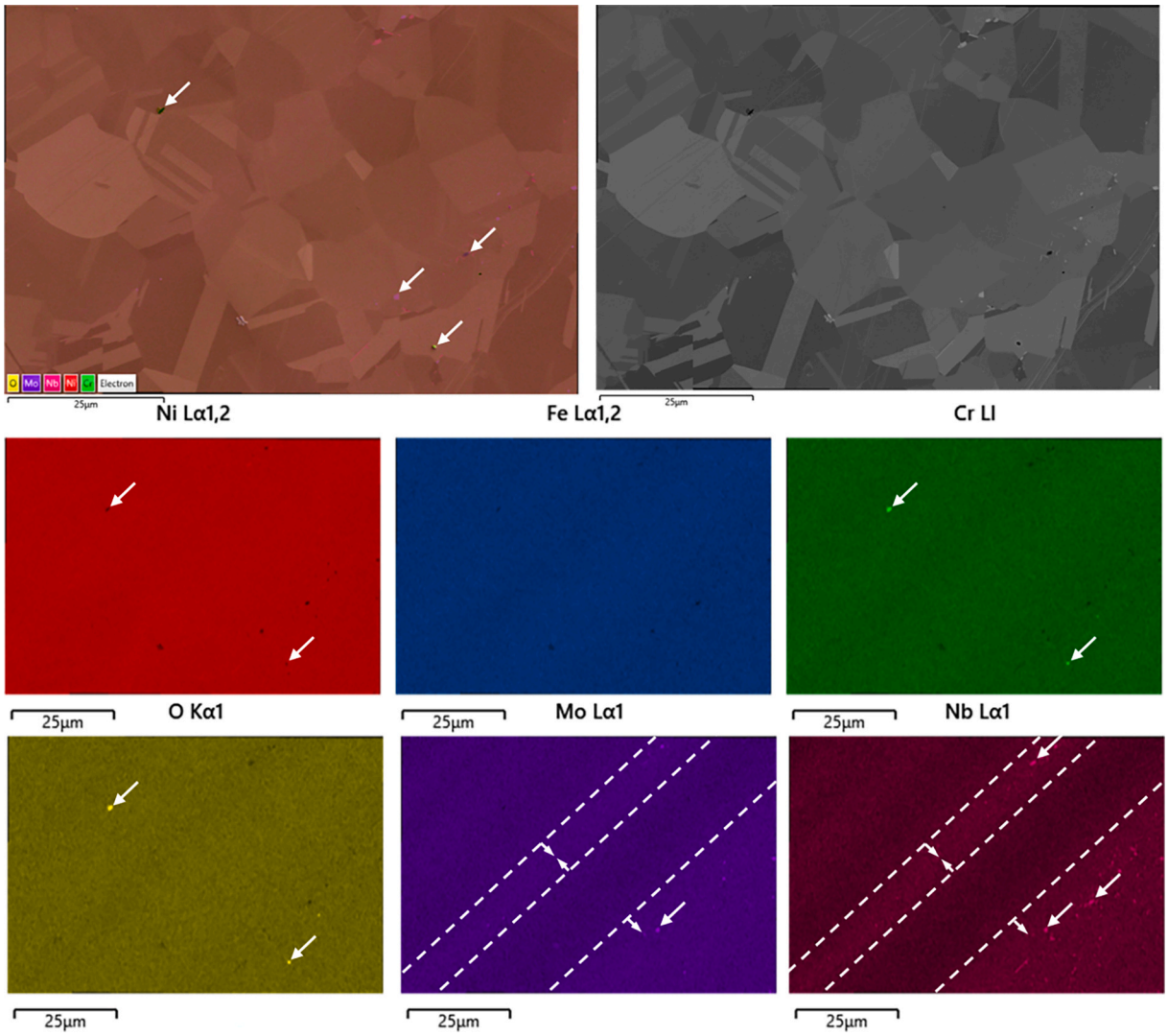

Fig. 2. SEM image and corresponding EDS elemental maps of the identical surface region of polished Inconel 625. Elemental distribution is color-coded as follows: red – nickel, blue – iron, green – chromium, yellow – oxygen, purple – molybdenum, and wine – niobium.

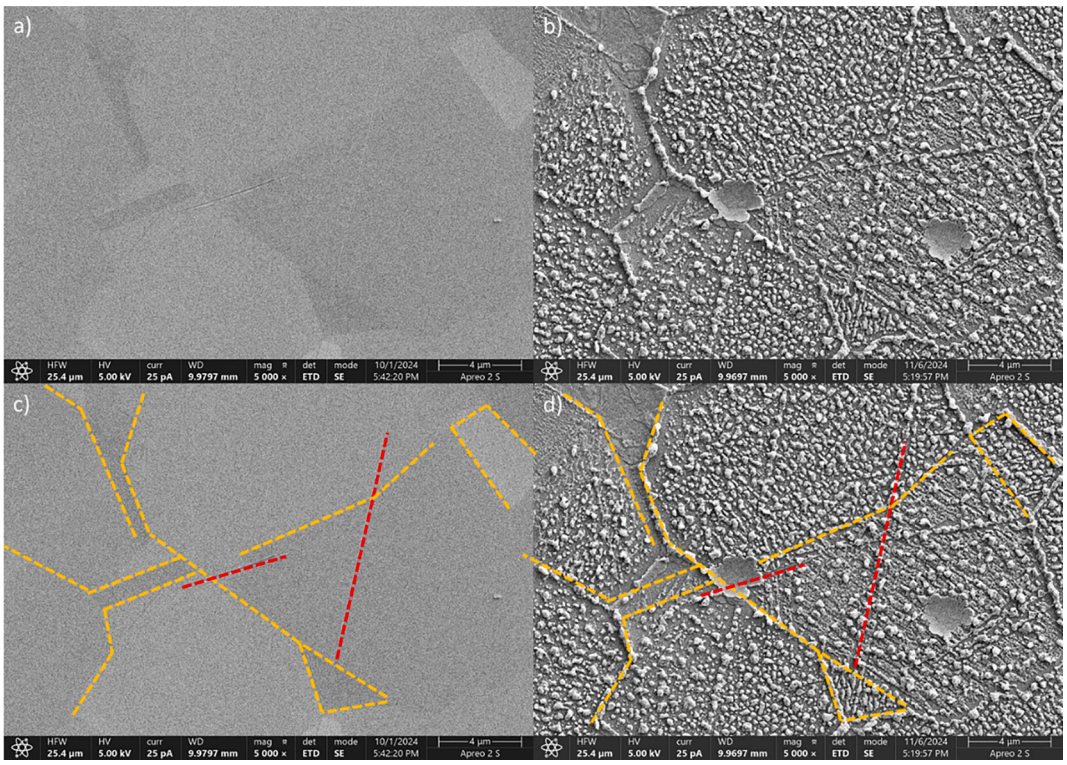

Fig. 3. IL-SEM images of polished Inconel 625 a, c) before and b,d) after nitridation. After nitridation, the formation of precipitates is observed at the grain boundaries marked with yellow dashed lines and scratches marked with a red dashed line in c) and d).

(Fig. 3 c,d). The nitridation process roughened the surface and induced elemental segregation. Notably, some grain boundaries exhibited greater precipitation, especially compared to scratches, while some remained visually intact (Fig. S3). XRD analysis (Fig. S2) identified the emergence of additional broad peaks, which can be attributed to the formation of chromium nitride (CrN) and possibly γ'-Ni_3Nb or other metastable nitride phases, indicating surface modification through nitrogen incorporation. As seen from EDS mapping analysis in Fig. 4, precipitates at grain boundaries are primarily enriched in Ni and Fe, but not in the form of nitrides and oxides, while Cr undergoes depletion. This is also in line with the following XPS and ToF-SIMS analysis. The observed precipitates are most likely δ-phase (Ni_3Nb, orthorhombic D0a), which typically nucleates preferentially along grain boundaries under such thermal conditions. According to the literature, δ-phase precipitation is commonly observed in Inconel 625 after short-term exposure to high temperatures [33]. Nevertheless, the presence of additional, finer precipitates inside the grains and occasional intragranular decorations suggests that γ″ phase (Ni_3Nb, body-centered tetragonal D022) may also be present. This is consistent with reports where δ-phase dominates grain boundaries, while γ″ precipitates form within the matrix during intermediate temperature exposures, resulting in a mixed precipitation behavior [34]. Furthermore, due to the significant Nb and Mo content in Inconel 625, the possible formation of secondary carbides, such as M_6C or MC-types, particularly at grain boundaries, cannot be excluded under these conditions. Such carbide phases have been reported to co-precipitate with δ-phase during thermal exposures in the 750–950 °C range, further contributing to grain boundary decoration [33].

3.3. Impact of anodic oxidation and OER electrochemistry on surface morphology and local composition

As observed in IL-SEM images (Fig. 5), anodic oxidation (AO) induces micrometer-scale intergranular corrosion (IGC) primarily along grain boundaries, where pronounced material etching occurred (Fig. 5c). In contrast, regions with pre-existing surface scratches (marked with red lines in Fig. 5) showed little to no material removal, indicating that these shallow defects did not penetrate deeply into the structure. More pronounced crack formation, particularly along grain boundaries, indicates deeper localized degradation, suggesting that the extent of IGC is closely tied to the compositional profile along the grain boundaries. After AO, EDS analysis confirmed that cracks were still enriched in Ni and Fe, while a significant depletion of Cr was also observed (Fig. 6, Fig. S5 and S6). This led to the spontaneous formation of an optimal surface Ni/Fe ratio of ~ 8:1 (Fig. S6), a composition known for enhancing OER activity [3–8]. The metals released into the electrolyte during AO are listed in Table S2. At the microscale, however, no significant morphological differences were observed (Fig. 5). XRD analysis (Fig. S2) shows a reduction in overall intensity and the absence of new crystalline oxide peaks, suggesting the formation of a predominantly amorphous or nanocrystalline oxide layer. The reduced intensity of Inconel peaks further implies partial dissolution or restructuring of the surface during the anodization process.

The observed intergranular corrosion (IGC) in Inconel 625 is primarily caused by the precipitation of δ-phase (Ni_3Nb), γ″ phase (Ni_3Nb), and carbides (e.g., M_xC) along grain boundaries during heat treatments [35]. Laves phase ($Ni_2(Nb,Mo)$) or (Fe_2Nb), however, forms only at high temperatures or after long exposures (thermal aging). These precipitates deplete chromium and molybdenum from adjacent zones, forming Cr-depleted regions that are prone to selective dissolution, similar to sensitization phenomena observed in stainless steels. Grain boundaries, as high-energy sites, further promote this process, accelerating IGC by facilitating micro-galvanic coupling [35]. After the OER measurement, Ni and Fe remained enriched at the cracks, although to a lesser extent. Interestingly, a localized increase in oxygen and chromium signals within the cracks was also observed, as indicated by the arrows in Fig. 6. We hypothesize that this increase in oxidized Cr originates from the interior of the alloy, where it had segregated during nitridation. Driven by selective surface dissolution and preferential oxidation of Ni and Fe, which do not redeposit locally, Cr becomes exposed. Notably, after the

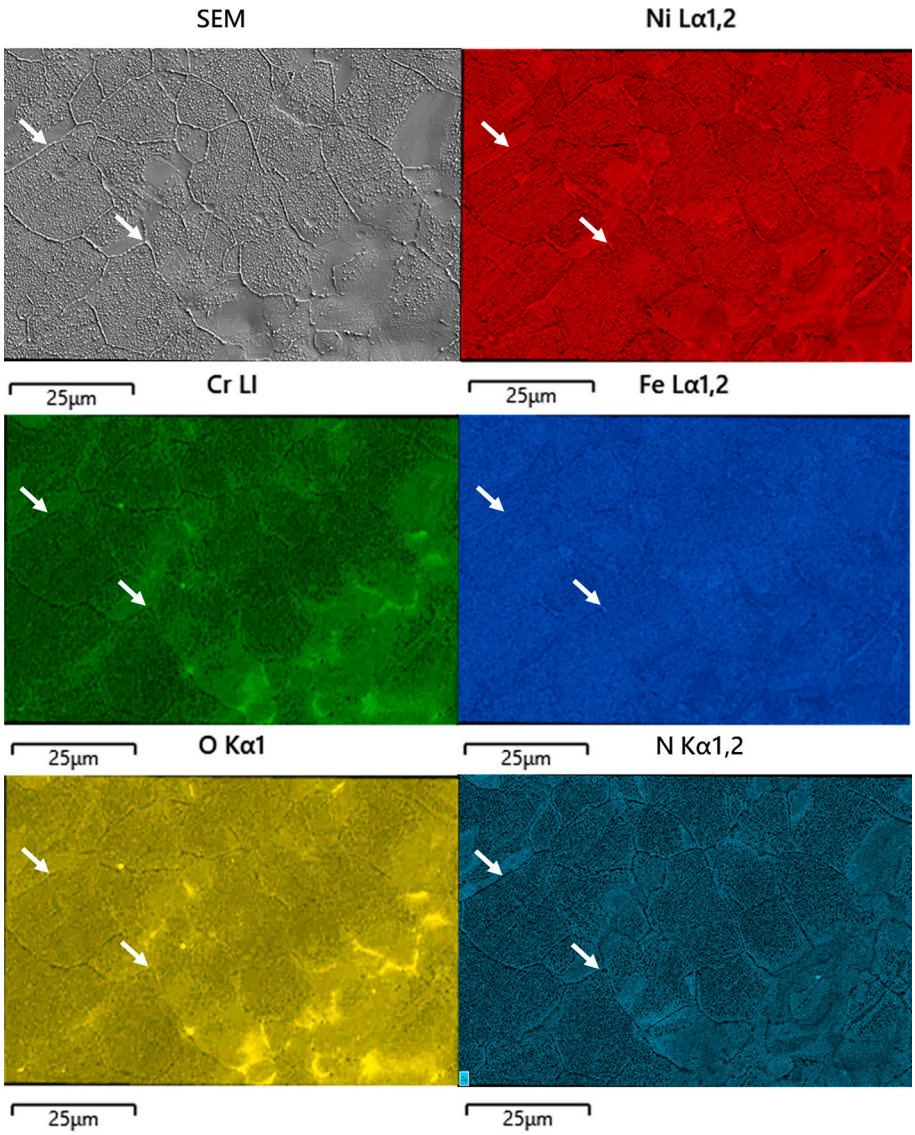

Fig. 4. SEM and EDS elemental mappings of Ni, Cr, Fe, O, and N on the identical surface region of nitrided Inconel 625. White arrows indicate a precipitate enriched in Ni and Fe, accompanied by a depletion of Cr, O, and N.

stability test (discussed later), the local elemental distribution remains preserved. However, the exact mechanism behind these observations remains unclear and requires further investigation.

A closer inspection of the SEM image in Fig. 5c reveals the formation of shallow micro-craters localized on individual grain facets. These features do not appear to correlate with pre-existing surface structures, suggesting their formation is not related to pre-existing topographical crystallographic features. Instead, they are likely influenced by local variations in the electric field and/or electrolyte composition during anodic oxidation, which may be inherently non-uniform across the surface. Additional supporting IL-SEM images are provided in the SI Fig. S4. Corrosion attack at the grain boundaries and the development of cracks are attributed to the depletion of Cr and enrichment of a less stable metal, such as Ni and Fe, at the grain boundaries following nitridation, as indicated by arrows in Fig. 4. Furthermore, the treatment increased surface roughness and porosity, increasing the electrochemically active surface area (ECSA) as shown later in the text.

The microstructure had a pronounced influence on morphology development during anodic oxidation and thus subsequent OER performance. Regions containing smaller grains, also referred to as segregation regions, exhibited significantly higher porosity formation [36]. This behavior is again most likely associated with chromium depletion at the grain boundaries, a phenomenon commonly observed in thermally treated Inconel alloys [35]. As a result, fine-grained regions are more susceptible to localized dissolution and IGC (Fig. 7, S6, S7, S8), consistent with previous reports showing that smaller grains exhibit higher corrosion rates [37]. The enhanced porosity in these areas contributed to an increase in electrochemically active surface area, thereby improving catalytic activity. In contrast, regions dominated by larger grains formed textured surfaces with deep and more defined cracks. These morphological features are believed to enhance oxygen bubble detachment efficiency at elevated current densities by creating more effective gas escape pathways, potentially reducing local mass transport limitations during OER operation [17,38]. Notably, EDS analysis confirmed that the Ni content remained consistent across both grain size regions (Fig. S6), suggesting that the observed differences in corrosion behavior and surface evolution are primarily driven by microstructural and compositional heterogeneities, particularly related to Cr distribution.

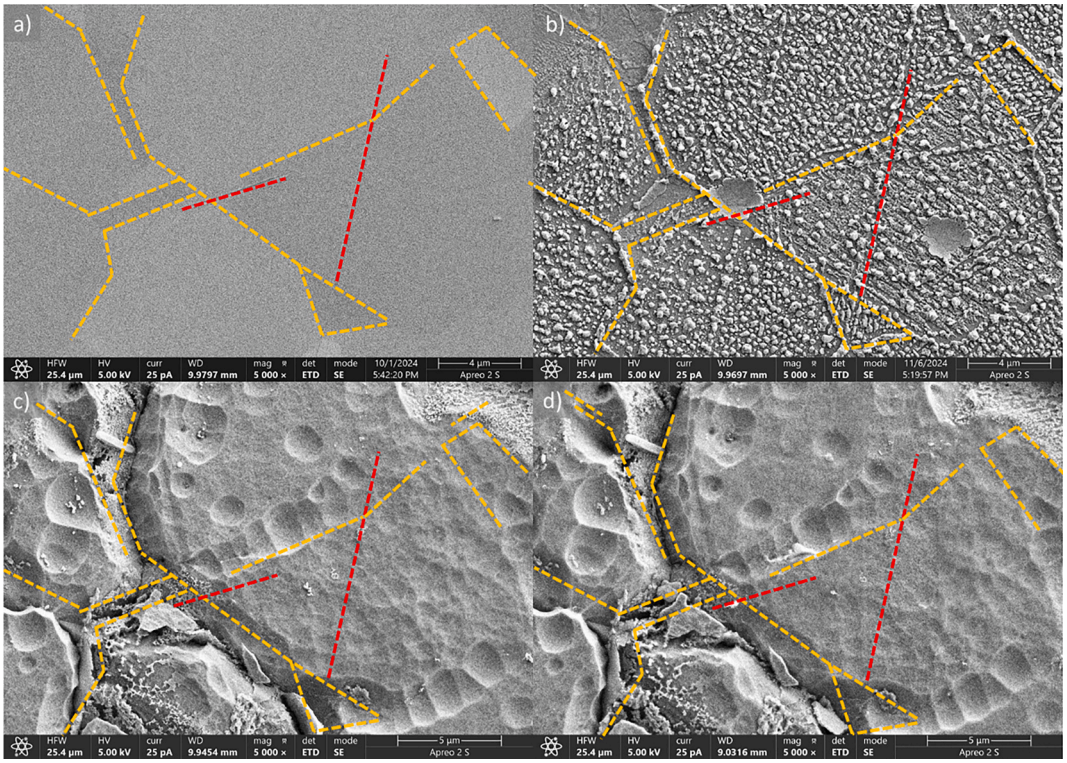

Fig. 5. IL-SEM of Inconel 625 a) before nitridation, b) after nitridation, c) after AO, and d) after OER electrochemical experiment. Marked dashed lines indicate grain boundaries (yellow) and scratches (red).

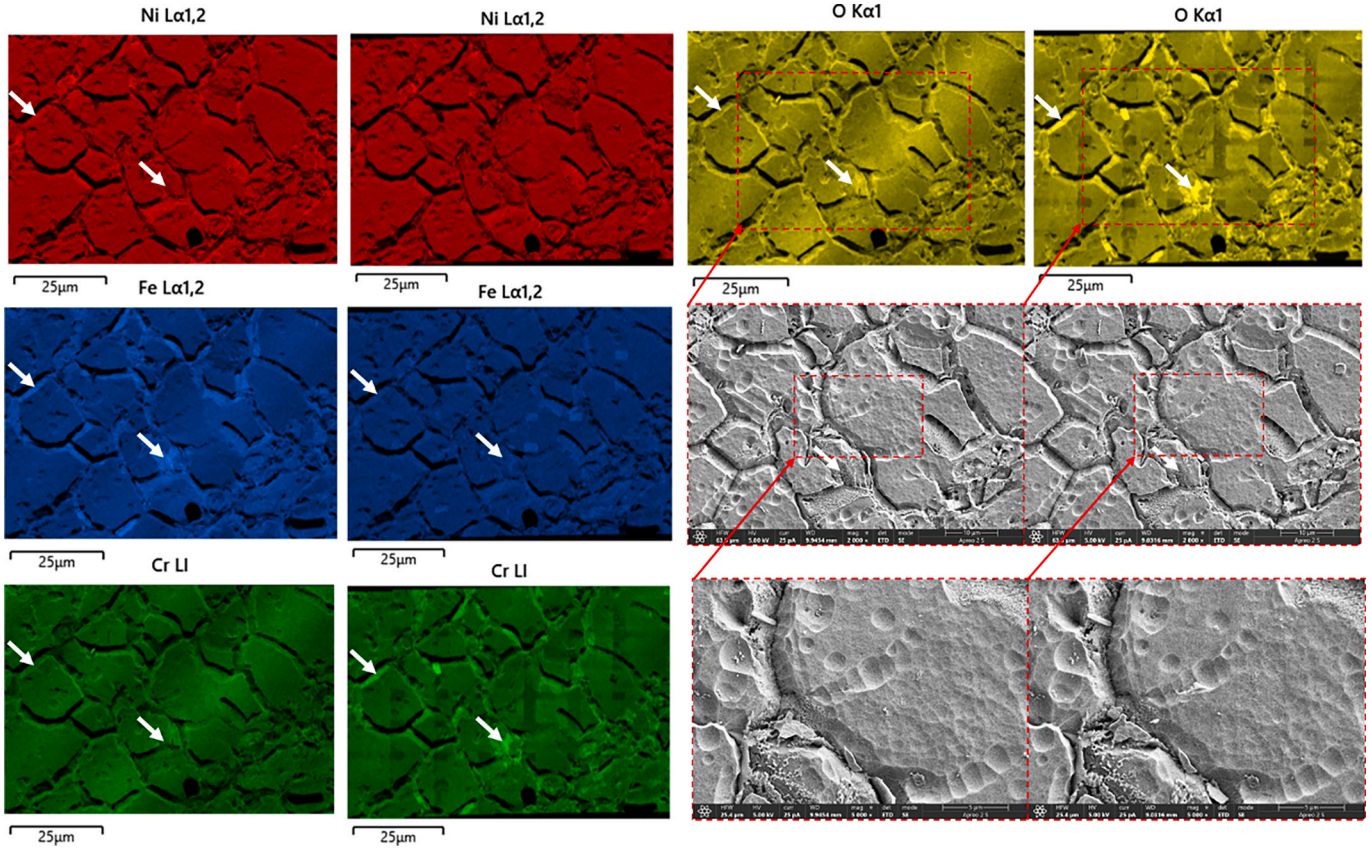

Fig. 6. EDS elemental mapping of Ni, Cr, Fe, O, and N on the identical surface region of polished Inconel 625 shown by SEM micrographs after AO and after OER electrochemistry. The white arrow at the region within the cracks before OER marks the local enrichment in Ni and Fe and depletion of Cr and O. After OER, O and Cr in the cracks exhibit growth while Fe exhibits slight depletion.

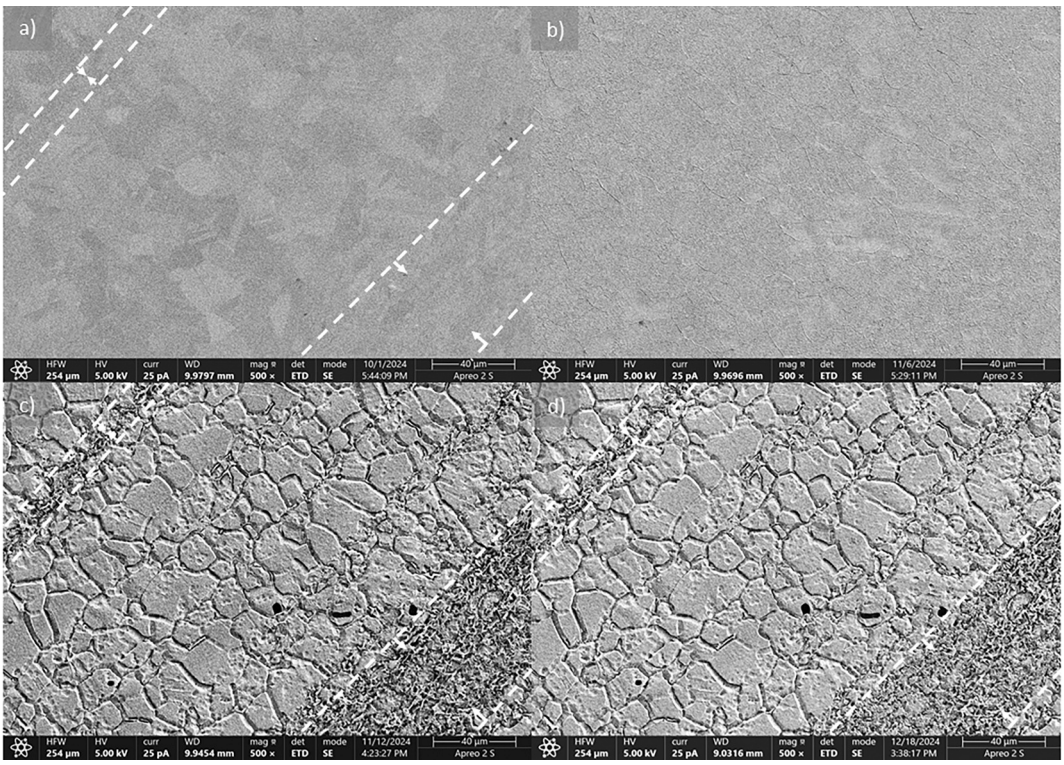

Fig. 7. IL-SEM of Inconel 625: a) before nitridation, b) after nitridation, c) after AO, and d) after OER electrochemical experiment. Marked dashed lines indicate regions with smaller grains and higher porosity formation.

3.4. Surface analysis using XPS, ToF-SIMS and XANES

XPS confirms the presence of all Inconel metals, namely Ni, Cr, Fe, Nb and Mo on all surfaces (Fig. 8a). After nitridation, the N 1s peak appears, indicating nitrogen incorporation. The intensity of the N 1s signal decreases significantly after anodic oxidation and becomes undetectable after OER (Fig. 8a), suggesting that nitrogen species are removed during these treatments, which is consistent with EDS analysis in Fig. 4. Besides metal oxides (feature at around 530 eV), an additional feature at approximately 531 eV suggests the presence of metal hydroxides (Fig. 8b). The high E_B side of the main O 1s peak can also correspond to oxidized carbonaceous species (as suggested in the C 1s spectra; Fig. S9). The Mo 3d spectrum (Fig. 8c) shows significant binding energy shifts. After nitridation, the dominant Mo $3d_{5/2}$ peak appears at 228.3 eV, which is attributed to MoO [39]. The shoulder on the more negative binding energy most likely corresponds to metallic Mo (Fig. S10a). Following AO, MoO undergoes oxidation, shifting Mo $3d_{5/2}$ peak to 232.3 eV, corresponding to Mo(VI) (Fig. S10b) [40,41]. After OER electrochemistry, Mo is no longer detected, indicating its removal from the topmost position. The Ni $2p_{3/2}$ spectra were fitted as suggested previously by Biesinger et al. [42]. The Ni 2p spectrum (Fig. 8d) suggests that after NT, the surface is mainly composed of metallic Ni (Fig. S10c, while some Ni-hydroxide is also present), as also observed in Fig. 4. However, after anodic oxidation and OER, Ni-hydroxide form (Figs. S10d,e), indicating progressive oxidation of the Ni surface, consistent with EDS analysis in Fig. 6, where the oxygen signal is increased, especially in cracks after OER. Cr species are observed only after nitridation (Fig. 8e). The position of the Cr 2p peaks corresponds to Cr_2O_3 with some metallic Cr also being present on the surface (Fig. S10f). After anodic oxidation and OER, Cr is absent in the topmost position, which is consistent with EDS analysis, where the Cr signal was observed only in the cracks (Fig. 6). The Cr $2p_{3/2}$ spectrum in Fig. S10f was fitted as suggested previously by Biesinger et al. [42]. The Fe 2p spectra suggest a low overall surface concentration of Fe species (Fig. 8f, note the non-normalized spectra). After nitridation, a peak at approximately 710.7 eV corresponds to oxidized Fe species. However, the Fe 2p signal interpretation is complicated by overlapping XPS-induced Ni LMM Auger peaks (Fig. 8a), which may contribute to this spectral feature. After the OER, this peak is significantly less intense, suggesting a lower surface concentration of this Fe species in the topmost position. Cs-related peaks in Fig. 8a are attributed to the previous ToF-SIMS sputtering procedure involving a Cs^+ sputter source rather than an intrinsic component of the analyzed surfaces. The K, F, and Na most likely originate from the AO or OER experiment electrolytes or from other sources of contamination. The detected carbon-containing species primarily comprise C–C/C–H and COO/COOH, likely originating from adventitious carbonaceous contamination (Fig. S9).

For the nitridated sample, Mo species were primarily identified as oxides using XPS analysis. Thus, the MoO^- signal was utilized for both nitridation and anodic oxidation samples to characterize the spatial distribution of these oxides in 3D ToF-SIMS images (Fig. 9). After OER, Mo was no longer detected via XPS, suggesting its near-complete removal or substantial depletion from the surface, which is consistent with the instability of molybdenum in alkaline solution [43]. Despite this, the presence of Mo^- in the ToF-SIMS images confirms that Mo remains in trace amounts, likely embedded within the surface layer. The detection of Mo-species after OER was only possible with ToF-SIMS, as it has a significantly lower detection limit than XPS (the surface atomic concentration of Mo is probably below 0.1 at.%). To represent Ni-related species, 3D ToF-SIMS images were obtained using the signal for Ni^-, which can originate from metallic Ni as well as other Ni-related species. After anodic oxidation and OER, progressive oxidation into hydroxides was determined by XPS and is consistent with the formation of the OER active film as reported previously [3–5,7,8]. Accordingly, 3D ToF-SIMS images were obtained by employing the $NiOH^-$ signal that predominantly originates from Ni-hydroxides (however, the $NiOH^-$ signal can also originate from Ni oxide) [40]. After nitridation, XPS analysis revealed that Cr is mainly present as Cr_2O_3. To show the distribution of these species, 3D ToF-SIMS images were obtained using the CrO_2^- signal.

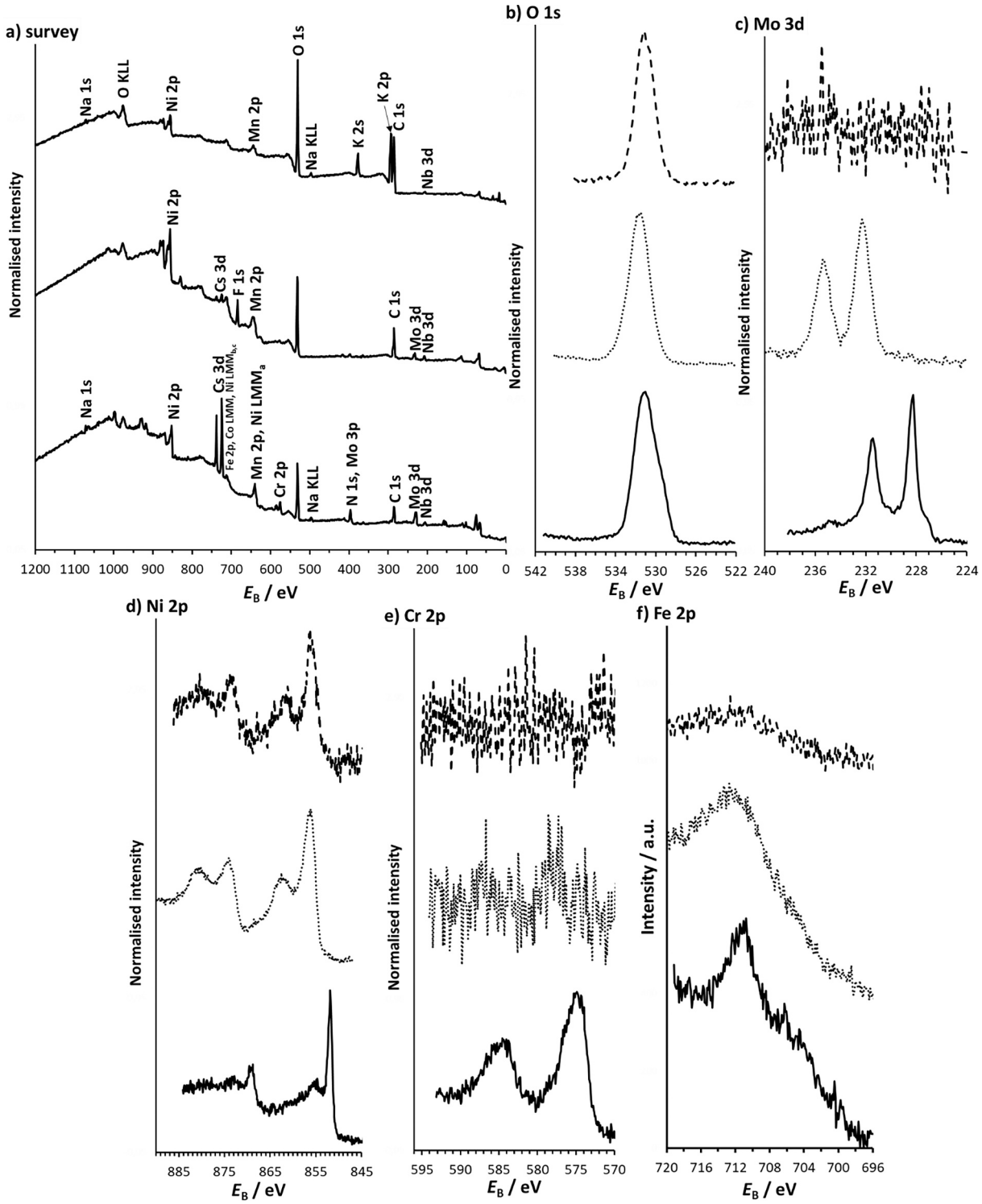

Fig. 8. Survey and high-resolution XPS spectra: a) survey, b) O 1s, c) Mo 3d, d) Ni 2p, e) Cr 2p, and f) Fe 2p. The lowest spectra correspond to the sample after NT, the middle spectra represent the sample after AO, and the highest spectra correspond to the sample after EC.

Additionally, for samples after anodic oxidation and OER, the Cr^- signal was employed to show the distribution of the Cr-related species (the same reason as for the Mo-species, as explained above). Cr shows a less homogeneous distribution across the surface compared to Ni, which is consistent with the above-described increase of local concentration of Cr in the cracks (Fig. 6) and in line with the intergranular corrosion mechanism. Fe-oxides and Nb-oxides/hydroxides were characterized by FeO_2^- and NbO_2^- signals, providing insight into their distribution across the samples. Both Fe- and Nb-related oxidized species are present on all three surfaces. This observation supports the established understanding that only a small amount of surface Fe is needed to enhance the OER activity of Ni-oxyhydroxide catalysts [6].

Fe and Ni K-edge XANES results, presented in Table S1 and Figs. S11 and S12, support the above observations. The spectra clearly reveal the presence of specific oxidation states of Fe and Ni cations and consistent trends induced by nitridation and anodic oxidation treatments. In the

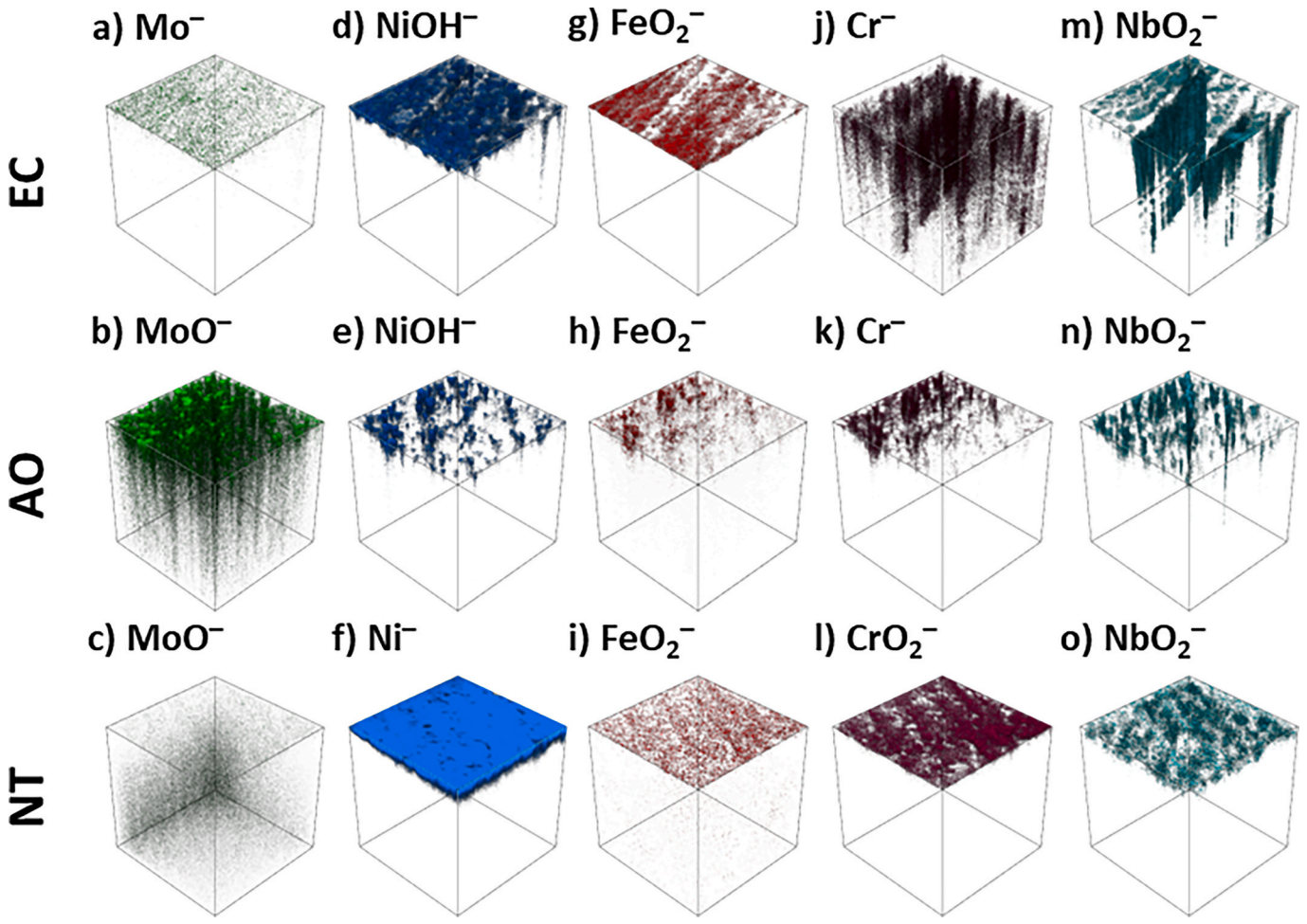

Fig. 9. 3D ToF-SIMS images obtained during sputtering of NT, AO, and EC samples showing a–c) Mo-related signals, d–f) Ni-related signals, g–i) Fe-related signals, j–l) Cr-related signals, and m–o) Nb-related signals. Square dimensions are 300 times 300 μm in x and y.

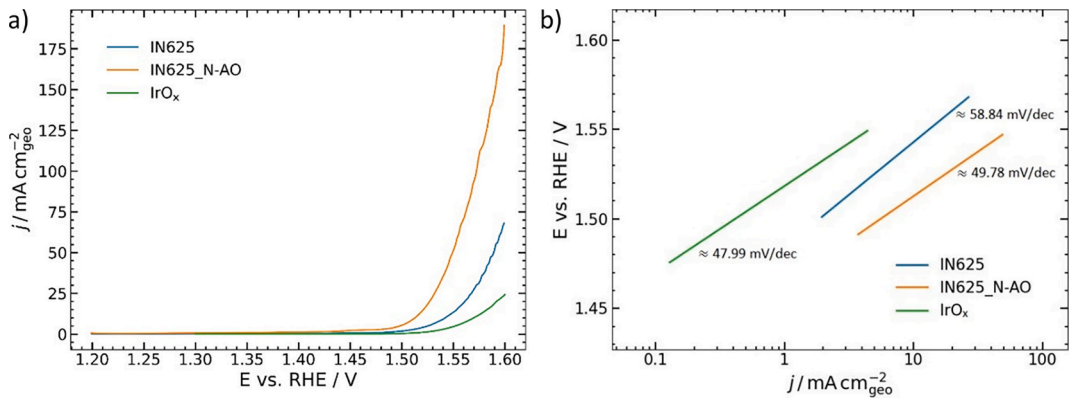

Fig. 10. a) OER performance analysis, including b) polarization curves and tafel slope evaluation, of untreated and modified inconel 625 compared to a commercial IrO_x catalyst.

100 nm thick surface layer of the polished Inconel disc, approximately 30 % of Fe cations are in the oxidized state, predominantly as Fe^{3+}, while the remaining 70 % are metallic. After treatment, the fraction of oxidized Fe increases to ~ 40 %, with 60 % remaining metallic. For Ni, the pristine surface is composed almost entirely of metallic Ni, with a minor NiO contribution (~4%). Post-treatment, ~15 % of Ni is oxidized, mainly to Ni^{2+}, with ~ 4 % as Ni^{3+}, while ~ 85 % remains metallic. Notably, Ni^{2+} is typically present in the pristine or ex-situ resting state of NiFe oxyhydroxide and is re-oxidized to Ni^{3+} under OER conditions. Due to the ~ 100 nm probing depth of the TEY detection mode, the XANES spectra reflect not only the modified Inconel surface but likely also a portion of the bulk material. For further details, please refer to the Experimental section.

3.5. *Electrochemical performance evaluation*

The electrochemical analysis demonstrated a marked improvement in OER activity for treated Inconel 625, as shown in Fig. 10a.

Polarization curves showed a reduction of approximately 40 mV in overpotential relative to the untreated Inconel disc, while Tafel slope analysis indicated improved reaction kinetics, reflecting more favorable charge transfer processes. We note that the untreated sample is in line with the performances measured in the literature, exhibiting 10 mA/cm^2 at 1.55 V vs. RHE [3]. Electrochemical surface area (ECSA) was estimated via electrochemical double layer capacitance measurements (C_{dl}) that demonstrated more than fourfold increase (Fig. S13), which is in accordance with the observed improvement in catalytic performance. Normalization of the OER polarization curves to the C_{dl} values confirms that the surfaces exhibit comparable specific activity (Fig. S14). Nonetheless, differences in mass transport behavior and bubble dynamics may still significantly affect the measured performance and must be considered in the interpretation. EIS Nyquist plot (Fig. S14) further confirmed a significant reduction in charge transfer resistance for the treated Inconel 625 (IN625_N_AO), as evidenced by the smaller semicircle compared to untreated IN625. Additionally, a slight decrease in high-frequency intercept on the real axis suggests lower internal electrolyte resistance, which may result from improved bubble removal dynamics during operation at 1.55 V vs. RHE. Low concentration of metal ions was determined in the electrolyte (Table S3), however, the anode material was stable. This is confirmed by the SEM analysis, where no morphological changes in the materials were observed (Figs. 5, 6, 7, S4, S6, S7, and S8). In terms of composition, some local oxidation was observed, where, after OER, O and Cr signals in the cracks exhibit further growth and Fe exhibits some depletion (Figs. 6, S5, and S6). Notably, the treated alloy significantly outperformed commercial IrO_x in OER performance, underscoring its potential as a cost-effective and scalable AWE anode material (Fig. 10a). For comparison, we evaluated the OER performance of samples that underwent only nitridation and anodic oxidation as separate steps. Both treatments resulted in poor activity, as shown in Fig. S14.

Additionally, stability was evaluated by applying a current density of 10 mA cm^{-2} for 96 h to IN625_N_AO. Interestingly, no degradation in OER activity was observed (Fig. S14). On the contrary, we observed a decrease in charge transfer resistance and a doubling of the electrochemically active surface area (ECSA), as shown in Fig. S15 and S8. These results are consistent with findings from Chatenet's group, which reported dynamic stabilization of similar systems during extended operation [3]. Morphologically, no significant changes were observed at low magnifications. However, upon closer inspection at higher magnifications, we detected the formation of pores and $Ni(OH)_2$/NiOOH nanoflakes or nanosheets, features that correlate well with the observed increase in ECSA. Such structures have indeed been reported previously [5]. Compositionally anode was further oxidized and Cr, Mo and Nb continued to dissolve, while Ni, Fe N remained relatively unaffected (Fig. S17). Local distribution of elenets did not change according to the IL-EDS mapings (Fig. S18).

4. Conclusion

This study demonstrated the successful activation of commercially available Inconel 625 into a high-performance OER anode through a combination of nitridation and anodic oxidation. The nitridation process induced NiFe enrichment and Cr depletion at grain boundaries, significantly affecting subsequent treatments. Anodic oxidation further restructured the catalytic surface by creating localized cracks and some micrometer-scale craters and established a surface NiFe ratio of approximately 8:1, a critical parameter for optimized OER activity. Regions with smaller grains exhibited higher porosity, contributing to an increased active surface area, while larger grains promoted the formation of textured regions with deeper cracks, improving oxygen bubble detachment efficiency. Electrochemical analysis revealed that the treated Inconel 625 outperformed commercial IrO_x in activity, with a twofold increase in the electrochemical surface area. Furthermore, after the 96-hour chronopotentiometry stability test, OER activity was retained, highlighting the exceptional stability of this material. IL-SEM and IL-EDS analyses provided valuable insights into the microstructural evolution during the treatments, highlighting the interplay between grain size, porosity, and catalytic performance. These findings establish commercial Inconel 625 as a prospective candidate for alkaline water electrolyzers, bridging the gap between performance, availability, and scalability. Future work will focus on refining surface and electrochemical treatment protocols to enhance surface properties, optimizing grain size and distribution, reducing Ni content in the native alloy and maximizing Cr removal to improve industrial applicability. The scalability and affordability of this approach offer significant potential for advancing industrial hydrogen production technologies.

CRediT authorship contribution statement

Luka Suhadolnik: Writing – review & editing, Writing – original draft, Visualization, Software, Methodology, Investigation, Funding acquisition, Formal analysis, Data curation, Conceptualization. **Črtomir Donik:** Writing – review & editing, Writing – original draft, Visualization, Validation, Software, Methodology, Investigation, Formal analysis, Data curation, Conceptualization. **Blaž Tomc:** Methodology, Investigation, Data curation. **Mejrema Nuhanović:** Visualization, Investigation, Data curation. **Martin Šala:** Methodology, Investigation, Data curation. **Marjan Bele:** Writing – review & editing, Methodology, Investigation, Formal analysis, Conceptualization. **Matjaž Finšgar:** Writing – review & editing, Writing – original draft, Visualization, Software, Methodology, Investigation, Formal analysis, Data curation. **Andraž Mavrič:** Writing – review & editing, Investigation, Formal analysis, Data curation. **Iztok Arčon:** Writing – review & editing, Visualization, Investigation, Formal analysis, Data curation. **Matjaž Godec:** Writing – review & editing, Supervision, Project administration, Funding acquisition. **Nejc Hodnik:** Writing – review & editing, Writing – original draft, Visualization, Supervision, Project administration, Methodology, Investigation, Funding acquisition, Formal analysis, Data curation, Conceptualization.

Declaration of competing interest

The authors declare that they have no known competing financial interests or personal relationships that could have appeared to influence the work reported in this paper.

Acknowledgments

The provision of financial support for the research and the preparation of the manuscript by the Slovenian Research and Innovation Agency (ARIS) within the research programs P2-0393, P2-0132, P2-0118, P2-0132, P2-0412, P1-0112, I0–0003 and I0-0006 and the projects GC-0004, MN-0022, N2-0155, N2-0248, N2-0337, J7-4636 and J7-50227 are gratefully acknowledged. We also acknowledge NATO Science for Peace and Security Program (Grant G6230) and SOLEIL synchrotron facility in Paris, France, for provision of beamtime for XAS experiments on Samba beamline (project 20240622) and we would like to thank Dr. Andrea Zitolo and Mr. Guillaume Alizon for their assistance in using beamline SAMBA. L. S. acknowledges ARIS project MN-0022. The project is co-financed by the Republic of Slovenia, the Ministry of Education, Science and Sport, and the European Union under the European Regional Development Fund. The authors acknowledge partial support from the Republic of Slovenia, the Ministry of Higher Education, Science and Innovation, and the European Union – NextGenerationEU in the framework of the project HyBReED, part of the Slovenian Recovery and Resilience Plan. Views and opinions expressed are however those of the authors only and do not necessarily reflect those of the Republic of Slovenia, the Ministry of Higher Education, the European Union, or the European Commission. Neither the Republic of Slovenia, the Ministry of Higher Education, Science and Innovation, the European Union nor the European Commission can be held responsible for them.

Appendix A. Supplementary data

Supplementary data to this article can be found online at https://doi.org/10.1016/j.apsusc.2025.164274.

Data availability

Data will be made available on request.

References

[1] N.S. Lewis, D.G. Nocera, Powering the planet: Chemical challenges in solar energy utilization, Proc. Natl. Acad. Sci. 103 (2006) 15729–15735. 10.1073/pnas.0603395103.

[2] J.O. Bockris, The origin of ideas on a Hydrogen Economy and its solution to the decay of the environment, Int. J. Hydrogen Energy 27 (2002) 731–740, https://doi.org/10.1016/S0360-3199(01)00154-9.

[3] L. Magnier, G. Cossard, V. Martin, C. Pascal, V. Roche, E. Sibert, I. Shchedrina, R. Bousquet, V. Parry, M. Chatenet, Fe–Ni-based alloys as highly active and low-cost oxygen evolution reaction catalyst in alkaline media, Nat. Mater. 23 (2024) 252–261, https://doi.org/10.1038/s41563-023-01744-5.

[4] M.W. Louie, A.T. Bell, An investigation of thin-film Ni–Fe oxide catalysts for the electrochemical evolution of oxygen, J. Am. Chem. Soc. 135 (2013) 12329–12337, https://doi.org/10.1021/ja405351s.

[5] F. Dionigi, P. Strasser, NiFe-based (Oxy)hydroxide catalysts for oxygen evolution reaction in non-acidic electrolytes, Adv. Energy Mater. 6 (2016) 1600621, https://doi.org/10.1002/aenm.201600621.

[6] D.Y. Chung, P.P. Lopes, P. Farinazzo Bergamo Dias Martins, H. He, T. Kawaguchi, P. Zapol, H. You, D. Tripkovic, D. Strmcnik, Y. Zhu, S. Seifert, S. Lee, V. R. Stamenkovic, N.M. Markovic, Dynamic stability of active sites in hydr(oxy) oxides for the oxygen evolution reaction, Nat. Energy 5 (2020) 222–230, https://doi.org/10.1038/s41560-020-0576-y.

[7] D. Friebel, M.W. Louie, M. Bajdich, K.E. Sanwald, Y. Cai, A.M. Wise, M.-J. Cheng, D. Sokaras, T.-C. Weng, R. Alonso-Mori, R.C. Davis, J.R. Bargar, J.K. Nørskov, A. Nilsson, A.T. Bell, Identification of highly active Fe sites in (Ni,Fe)OOH for electrocatalytic water splitting, J. Am. Chem. Soc. 137 (2015) 1305–1313, https://doi.org/10.1021/ja511559d.

[8] S. Klaus, Y. Cai, M.W. Louie, L. Trotochaud, A.T. Bell, Effects of Fe electrolyte impurities on Ni(OH)2/NiOOH structure and oxygen evolution activity, J. Phys. Chem. C 119 (2015) 7243–7254, https://doi.org/10.1021/acs.jpcc.5b00105.

[9] I. Katsounaros, S. Cherevko, A.R. Zeradjanin, K.J.J. Mayrhofer, Oxygen electrochemistry as a cornerstone for sustainable energy conversion, Angew. Chem. Int. Ed. 53 (2014) 102–121, https://doi.org/10.1002/anie.201306588.

[10] M.L.S. Nielsen, J. Rossmeisl, 12 - High-entropy alloys for catalysis, in: G. Yasin, M. A. Khan, M.A. Afifi, T.A. Nguyen, Y. Zhang (Eds.), High-Entropy Alloys, Elsevier, 2024: pp. 267–288. 10.1016/B978-0-443-22142-2.00012-0.

[11] V.R. Stamenkovic, B. Fowler, B.S. Mun, G. Wang, P.N. Ross, C.A. Lucas, N. M. Marković, Improved oxygen reduction activity on Pt3Ni(111) via increased surface site availability, Science 315 (2007) (1979) 493–497, https://doi.org/10.1126/science.1135941.

[12] Z.W. Seh, J. Kibsgaard, C.F. Dickens, I. Chorkendorff, J.K. Nørskov, T.F. Jaramillo, Combining theory and experiment in electrocatalysis: Insights into materials design, Science (1979) 355 (2017) eaad4998. 10.1126/science.aad4998.

[13] V. Strotkötter, O.A. Krysiak, J. Zhang, X. Wang, E. Suhr, W. Schuhmann, A. Ludwig, Discovery of high-entropy oxide electrocatalysts: from thin-film material libraries to particles, Chem. Mater. 34 (2022) 10291–10303, https://doi.org/10.1021/acs.chemmater.2c01455.

[14] W.T. Hong, M. Risch, K.A. Stoerzinger, A. Grimaud, J. Suntivich, Y. Shao-Horn, Toward the rational design of non-precious transition metal oxides for oxygen electrocatalysis, Energy Environ. Sci. 8 (2015) 1404–1427, https://doi.org/10.1039/C4EE03869J.

[15] S. Trasatti, Work function, electronegativity, and electrochemical behaviour of metals: III. Electrolytic hydrogen evolution in acid solutions, J. Electroanal. Chem. Interfacial Electrochem. 39 (1972) 163–184, https://doi.org/10.1016/S0022-0728(72)80485-6.

[16] B.E. Conway, J.O. Bockris, Electrolytic hydrogen evolution kinetics and its relation to the electronic and adsorptive properties of the metal, J. Chem. Phys. 26 (1957) 532–541, https://doi.org/10.1063/1.1743339.

[17] A.R. Zeradjanin, A.A. Topalov, Q. Van Overmeere, S. Cherevko, X. Chen, E. Ventosa, W. Schuhmann, K.J.J. Mayrhofer, Rational design of the electrode morphology for oxygen evolution – enhancing the performance for catalytic water oxidation, RSC Adv. 4 (2014) 9579–9587, https://doi.org/10.1039/C3RA45998E.

[18] A.R. Kamšek, F. Ruiz-Zepeda, M. Bele, A. Logar, G. Dražić, N. Hodnik, Structure–stability relationships in Pt-alloy nanoparticles using identical-location four-dimensional scanning transmission electron microscopy and unsupervised machine learning, ACS Nano (2025), https://doi.org/10.1021/acsnano.4c12528.

[19] G. Koderman Podboršek, A.R. Kamšek, A. Lončar, M. Bele, L. Suhadolnik, P. Jovanovič, N. Hodnik, Atomically-resolved structural changes of ceramic supported nanoparticulate oxygen evolution reaction Ir catalyst, Electrochim Acta 426 (2022) 140800, https://doi.org/10.1016/j.electacta.2022.140800.

[20] X. Geng, M. Vega-Paredes, Z. Wang, C. Ophus, P. Lu, Y. Ma, S. Zhang, C. Scheu, C. H. Liebscher, B. Gault, Grain boundary engineering for efficient and durable electrocatalysis, Nat. Commun. 15 (2024) 8534, https://doi.org/10.1038/s41467-024-52919-w.

[21] D. Raabe, J.R. Mianroodi, J. Neugebauer, Accelerating the design of compositionally complex materials via physics-informed artificial intelligence, Nat. Comput. Sci. 3 (2023) 198–209, https://doi.org/10.1038/s43588-023-00412-7.

[22] L.J. Moriau, A. Hrnjić, A. Pavlišič, A.R. Kamšek, U. Petek, F. Ruiz-Zepeda, M. Šala, L. Pavko, V.S. Šelih, M. Bele, P. Jovanovič, M. Gatalo, N. Hodnik, Resolving the nanoparticles' structure-property relationships at the atomic level: a study of Pt-based electrocatalysts, Iscience 24 (2021), https://doi.org/10.1016/j.isci.2021.102102.

[23] X. Xu, Y. Zhong, M. Wajrak, T. Bhatelia, S.P. Jiang, Z. Shao, Grain boundary engineering: an emerging pathway toward efficient electrocatalysis, InfoMat 6 (2024) e12608, https://doi.org/10.1002/inf2.12608.

[24] J. Aarons, L. Jones, A. Varambhia, K.E. MacArthur, D. Ozkaya, M. Sarwar, C.-K. Skylaris, P.D. Nellist, Predicting the oxygen-binding properties of platinum nanoparticle ensembles by combining high-precision electron microscopy and density functional theory, Nano Lett. 17 (2017) 4003–4012, https://doi.org/10.1021/acs.nanolett.6b04799.

[25] L.A. Baker, Perspective and prospectus on single-entity electrochemistry, J. Am. Chem. Soc. 140 (2018) 15549–15559, https://doi.org/10.1021/jacs.8b09747.

[26] N. Hodnik, S. Cherevko, Spot the difference at the nanoscale: identical location electron microscopy in electrocatalysis, Curr. Opin. Electrochem. 15 (2019), https://doi.org/10.1016/j.coelec.2019.03.007.

[27] L.M. Gandía, R. Oroz, A. Ursúa, P. Sanchis, P.M. Diéguez, Renewable hydrogen production: performance of an alkaline water electrolyzer working under emulated wind conditions, Energy Fuel 21 (2007) 1699–1706, https://doi.org/10.1021/ef060491u.

[28] B. Ravel, M. Newville, ATHENA, ARTEMIS, HEPHAESTUS: data analysis for X-ray absorption spectroscopy using IFEFFIT, J. Synchrotron Radiat. 12 (2005) 537–541, https://doi.org/10.1107/S0909049505012719.

[29] I. Arčon, J. Kolar, A. Kodre, D. Hanžel, M. Strlič, XANES analysis of Fe valence in iron gall inks, X-Ray Spectrom. 36 (2007) 199–205, https://doi.org/10.1002/xrs.962.

[30] H.-T. Vu, I. Arčon, D.O. de Souza, S. Pollastri, G. Dražić, J. Volavšek, G. Mali, N. Zabukovec Logar, N. Novak Tušar, Insight into the interdependence of Ni and Al in bifunctional Ni/ZSM-5 catalysts at the nanoscale, Nanoscale Adv. 4 (2022) 2321–2331, https://doi.org/10.1039/D2NA00102K.

[31] R. Dominko, C. Sirisopanaporn, C. Masquelier, D. Hanzel, I. Arcon, M. Gaberscek, On the origin of the electrochemical capacity of Li2Fe0.8Mn0.2SiO4, J. Electrochem. Soc. 157 (2010) A1309, https://doi.org/10.1149/1.3491368.

[32] D.A. Skobir Balantič, Č. Donik, B. Podgornik, A. Kocijan, M. Godec, Improving the surface properties of additive-manufactured Inconel 625 by plasma nitriding, Surf. Coat. Technol. 452 (2023) 129130, https://doi.org/10.1016/j.surfcoat.2022.129130.

[33] X. Liu, J. Fan, P. Zhang, K. Cao, Z. Wang, F. Chen, D. Liu, B. Tang, H. Kou, J. Li, Influence of heat treatment on Inconel 625 superalloy sheet: carbides, γ'', δ phase precipitation and tensile deformation behavior, J. Alloys Compd. 930 (2023) 167522, https://doi.org/10.1016/j.jallcom.2022.167522.

[34] M. Anderson, A.-L. Thielin, F. Bridier, P. Bocher, J. Savoie, δ phase precipitation in Inconel 718 and associated mechanical properties, Mater. Sci. Eng. A 679 (2017) 48–55, https://doi.org/10.1016/j.msea.2016.09.114.

[35] L. Xu, J. Zhang, Y. Han, L. Zhao, H. Jing, Insights into the intergranular corrosion of overlay welded joints of X65-Inconel 625 clad pipe and its relationship to damage penetration, Corros. Sci. 160 (2019) 108169, https://doi.org/10.1016/j.corsci.2019.108169.

[36] C. Guo, M. Ying, H. Dang, R. Hu, F. Chen, Microstructural and intergranular corrosion properties of Inconel 625 superalloys fabricated using wire arc additive manufacturing, Mater. Res. Express 8 (2021) 35103, https://doi.org/10.1088/2053-1591/abe977.

[37] K.D. Ralston, N. Birbilis, C.H.J. Davies, Revealing the relationship between grain size and corrosion rate of metals, Scr. Mater. 63 (2010) 1201–1204, https://doi.org/10.1016/j.scriptamat.2010.08.035.

[38] A.J.G. Rea, A.L. Pauls, A.K. Taylor, B.D. Gates, Enhancing the performance of nickel electrocatalysts for the oxygen evolution reaction using arrays of self-cleaning linear ridges, ACS Appl. Energy Mater. 7 (2024) 3187–3200, https://doi.org/10.1021/acsaem.3c03187.

[39] A. V. Naumkin, A. Kraut-Vass, S.W. Gaarenstroom, C.J. Powell, NIST X-ray Photoelectron Spectroscopy Database, (n.d.).

[40] J. Baltrusaitis, B. Mendoza-Sanchez, V. Fernandez, R. Veenstra, N. Dukstiene, A. Roberts, N. Fairley, Generalized molybdenum oxide surface chemical state XPS determination via informed amorphous sample model, Appl. Surf. Sci. 326 (2015) 151–161, https://doi.org/10.1016/j.apsusc.2014.11.077.

[41] D.O. Scanlon, G.W. Watson, D.J. Payne, G.R. Atkinson, R.G. Egdell, D.S.L. Law, Theoretical and experimental study of the electronic structures of MoO3 and MoO2, J. Phys. Chem. C 114 (2010) 4636–4645, https://doi.org/10.1021/jp9093172.

[42] M.C. Biesinger, B.P. Payne, L.W.M. Lau, A. Gerson, R.St.C. Smart, X-ray photoelectron spectroscopic chemical state quantification of mixed nickel metal, oxide and hydroxide systems, Surf. Interface Anal. 41 (2009) 324–332, https://doi.org/10.1002/sia.3026.

[43] M. Pourbaix, Atlas of Electrochemical Equilibria in Aqueous Solutions, National Association of Corrosion Engineers (1974). https://books.google.si/books?id=QjxRAAAAMAAJ.